Chapter 6
Experimental Challenges of Shear Rheology: How to Avoid Bad Data

Randy H. Ewoldt, Michael T. Johnston, and Lucas M. Caretta

Abstract A variety of measurement artifacts can be blamed for misinterpretations of shear thinning, shear thickening, and viscoelastic responses, when the material does not actually have these properties. The softness and activity of biological materials will often magnify the challenges of experimental rheological measurements. The theoretical definitions of rheological material functions are based on stress, strain, and strain-rate components in simple deformation fields. In reality, one typically measures loads and displacements at the boundaries of a sample, and the calculation of true stress and strain may be encumbered by instrument resolution, instrument inertia, sample inertia, boundary effects, and volumetric effects. Here we discuss these common challenges in measuring shear material functions in the context of soft, water-based, and even living biological complex fluids. We discuss techniques for identifying and minimizing experimental errors and for pushing the experimental limits of rotational shear rheometers. Two extreme case studies are used: an ultrasoft aqueous polymer/fiber network (hagfish defense gel) and an actively swimming suspension of microalgae (*Dunaliella primolecta*).

1 Introduction

Rheological properties answer the question, "What happens when I poke it?" A complex material gives a complex answer, e.g., with properties that are functions, not constants.

For a rheologically complex fluid, there is no single value of viscosity or modulus, but instead the dissipative resistance to flow (viscosity) and elastic resistance to

R.H. Ewoldt (✉) • M.T. Johnston
Department of Mechanical Science and Engineering, University of Illinois at Urbana-Champaign, Urbana, IL 61801, USA
e-mail: ewoldt@illinois.edu; mjhnstn2@illinois.edu

L.M. Caretta
Department of Materials Science and Engineering, Massachusetts Institute of Technology, Cambridge, MA 02139, USA
e-mail: caretta@mit.edu

S.E. Spagnolie (ed.), *Complex Fluids in Biological Systems*, Biological and Medical Physics, Biomedical Engineering,
DOI 10.1007/978-1-4939-2065-5_6

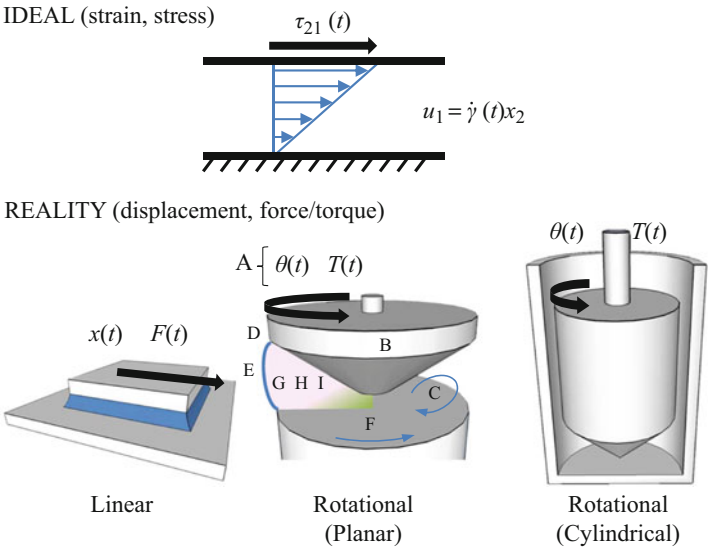

Fig. 6.1 Ideally, shear rheological properties are defined from strain $\gamma(t)$ and stress $\tau_{yx}(t)$ in homogeneous simple shear. In reality, boundary displacements and loads are measured and nonideal experimental artifacts must be considered. The effects labeled as (*A*)–(*I*) are particularly important with biological complex fluids, and include (*A*) resolution/range of measured load and displacement, (*B*) instrument inertia (if load and displacement are measured on same boundary), (*C*) fluid inertia and secondary flows, (*D*) surface tension, (*E*) free surface interfacial rheology, (*F*) slip at boundaries, (*G*) sample underfill or overfill, (*H*) small volume and gap, (*I*) nonhomogeneous sample from settling, migration, or rheotaxis

deformation (modulus) are functions of the loading time scale, loading amplitude, or other environmental factors including temperature, pressure, electromagnetic fields, or the internal activity of living biological systems. These function-valued rheological properties are known as *material functions* [1], and they form the language of descriptive rheology. The descriptive nomenclature is well defined for simple, ideal deformations [1], including simple shear (Fig. 6.1). The input can be either strain or stress, and different time-histories can be used, typically step functions or sinusoidal oscillations [2]. Of course, experimental conditions may be nonideal.

The big idea of this chapter is that properties are defined from ideal deformations (in terms of strain and stress), but experimental techniques measure displacements and loads (such as forces or torques), as outlined in Fig. 6.2. Assumptions are required to convert displacement to strain and, similarly, load to stress, and therein lies the risk that nonideal conditions exist as shown in Fig. 6.1. The effects labeled as (A)–(I) in Fig. 6.1 are particularly important with biological complex fluids and include (A) resolution/range of measured load and displacement, (B) instrument inertia (if load and displacement are measured on same boundary), (C) fluid inertia and secondary flows, (D) surface tension, (E) free surface interfacial rheology, (F) slip at boundaries, (G) sample underfill or overfill, (H) small volume and gap, and (I) non-homogeneous sample from settling, migration, or rheotaxis.

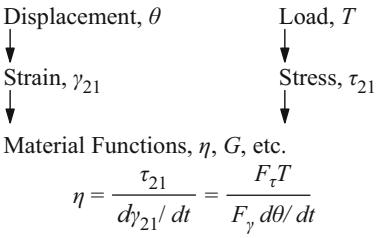

Fig. 6.2 Material properties are related to stress and strain, but these cannot be measured directly. The calculations from measured quantities require assumptions that are commonly violated, especially for biological fluids that tend to be either low viscosity, soft, or slippery. *Arrows* in figure indicate information flow into calculations. The road map is general. Example variables are shown for measuring shear properties with rotational devices

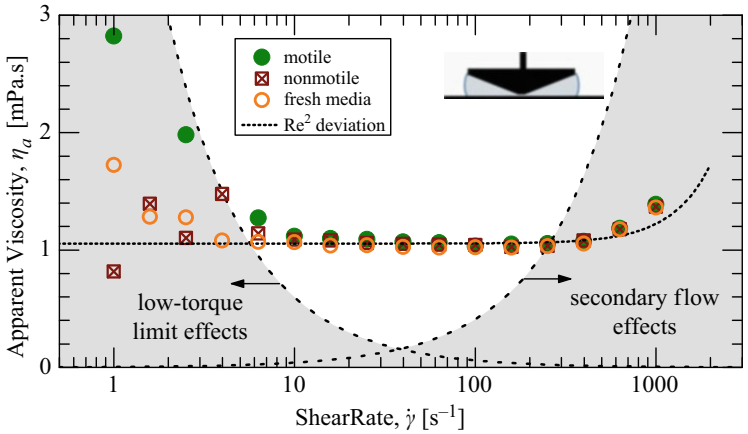

Fig. 6.3 Steady shear flow measurements could be misinterpreted as shear thinning and shear thickening if an experimental window is not identified. Here, shown with dilute suspensions of motile and nonmotile swimming microalgae *Dunaliella primolecta* compared to fresh media (no cells present). The low-torque limit, described in Sect. 3.1, is drawn from Eq. 6.13 using $T_{min} = 0.1$ μN.m. The secondary flow limit, described in Sect. 3.3, is drawn from Eq. 6.31 using $Re_{max} = 4$. The Re^2 line is from the expected increase in torque due to secondary flow, Eq. 6.29 (Previously unpublished work of authors RHE and LMC)

Nonideal conditions can translate to misinterpretations of results, such as the observation of apparent shear thinning and shear thickening for a fluid that is actually Newtonian within the range of test conditions, as shown in Fig. 6.3.

Figure 6.3 gives examples of rate-dependent shear viscosity measurements, which include data for a living system of microalgae suspended in water, as well as the media without cells. The data show shear thinning at low rates and shear thickening at high rates. But this is not actually the case for the true intensive material property! Note the gray regions in Fig. 6.3. These cover experimental limitations for measuring shear viscosity; in this case a measurement resolution issue at low rates,

and at high rates, nonideal flow conditions. Within the experimentally accessible window, i.e., the white central region, the fluids are more confidently interpreted as Newtonian. Such limitations are particularly present when measuring biological complex fluids, since they are often soft, with low viscosity, and may even have activity (such as the swimming microalgae here) or surface-active components that modify the liquid-air interface.

This chapter will outline a checklist and guide for believable experimental measurements, interpretations, and descriptions of complex fluid rheology. The checklist is useful for biological and nonbiological systems alike.

For proper context, two important ideas must be kept in mind. First, rheological material functions are universally applicable to any class of material. They are used to describe polymer liquids, polymer solids, colloidal systems, and any other simple or complex structured fluid of the past, present, or future, so long as the continuum hypothesis is satisfied for the lengthscale of interest. Like other material properties, definitions are independent of the underlying structure (polymeric, colloidal, etc.), yet, the underlying structure can be related to the measured properties through structure-property relations specific to material classes [3]. Second, we note that the *descriptive* material functions resulting from measurements are not necessarily *predictive* for more complex deformations, although there are certain limiting cases where there is correspondence between descriptive material functions and predictive tensorial constitutive equation parameters [4]. Material functions are of course used to fit existing models (see Chap. 1 of this book) or used to motivate new constitutive models.

Here we focus on measurements and the corresponding descriptive quantities. Of course, such measurements are often used for either structure-property relations or model selection/fitting of predictive constitutive models. For those follow-up steps to be successful, the measurements must first be free from errors.

Avoiding bad data is a serious challenge with complex fluids in general and soft biological fluids in particular. Throughout this chapter, three key materials will serve as examples of soft, watery, or active fluids. This includes (i) actively swimming microalgae in a suspension of aqueous media (Fig. 6.3) (see also Chap. 9 of this book on active suspensions), (ii) a biopolymer hagfish defense gel (Fig. 6.4), which involves mucin-like molecules (see Chap. 2 of this book for a discussion of mucins), and (iii) water itself, which is the basis of biological fluids. Material details are outlined in the appendix.

2 Background: Material Functions

The theoretical definitions of material functions are based on stress, strain, and strain-rate components in simple deformation fields. (See Chap. 1 of this book for additional background on stress, and strain-rate tensors.) With real measurements, one typically measures loads and displacements at the boundaries of a sample (Fig. 6.1), and the calculation of true stress and strain may be encumbered by

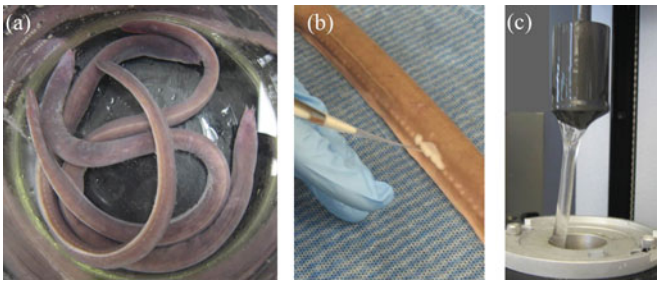

Fig. 6.4 Hagfish defense gel (a.k.a. slime) is one extreme case study used here to outline experimental rheology challenges. Hagfish produce heroic amounts of slime as a predatory defense mechanism, using a very small amount of exudate (0.01 wt% of final gel mass); (**a**) top-down view of three Atlantic hagfish (*Myxine glutinosa*) in a large glass beaker; (**b**) for experiments, exudate can be collected from an anesthetized hagfish with a pipette and then mixed with seawater to form "hagfish slime," an ultra-dilute network of polymeric mucus and fibrous protein-based intermediate filament threads, shown in (**c**) with a rotational rheometer geometry in the raised position after testing (diameter 28 mm). The ultrasoft material pushes experimental limits of low torque, instrument inertia, and sample inertia; measurements also demonstrate interio-elastic ringing (Figure adapted from [5])

the issues labeled A–I in Fig. 6.1. This chapter summarizes key experimental challenges for complex fluids, especially for biological fluids. These experimental challenges may invalidate results and sometimes cause measured properties to incorrectly *appear* nonlinear or non-Newtonian. A useful approach is to identify the experimental windows for proper measurements (Figs. 6.3, 6.5, 6.6, 6.10, 6.11, 6.14, and 6.15). The boundaries of these figures will be described in Sect. 3.

Here we will focus on simple shear deformation, rather than shear-free flows, although many of the experimental challenges will also affect measurements of extensional properties. Ideal simple shear characterization is defined by the velocity field $u = e_1 \dot{\gamma}(t) x_2$, giving a homogeneous rate of deformation tensor

$$\dot{\gamma} = \begin{pmatrix} 0 & \dot{\gamma}(t) & 0 \\ \dot{\gamma}(t) & 0 & 0 \\ 0 & 0 & 0 \end{pmatrix}. \tag{6.1}$$

In principle, Eq. 6.1 results in a spatially homogeneous stress tensor

$$\sigma = \begin{pmatrix} -p + \tau_{11}(t) & \tau_{21}(t) & 0 \\ \tau_{21}(t) & -p + \tau_{22}(t) & 0 \\ 0 & 0 & -p + \tau_{33}(t) \end{pmatrix}, \tag{6.2}$$

where symmetry arguments have been used to limit the number of independent stress quantities.

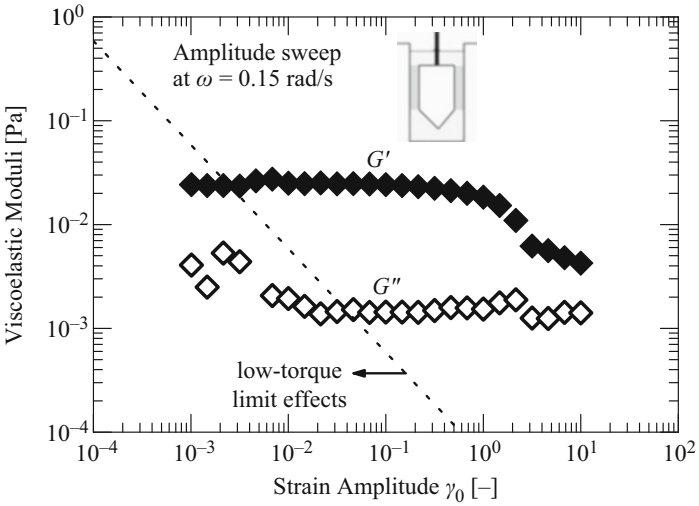

Fig. 6.5 Low-torque limit shown for oscillatory strain-amplitude sweep of hagfish gel. The experimental boundary helps identify the most believable data and explains the increased measurement variability of G'' compared to G' at the same strain amplitude. Low-torque limit drawn from Eq. 6.14 using $T_{\min} = 0.003$ μN.m (Data originally published in [5])

Material functions are then defined by reporting an *output* normalized by an *input* amplitude. The controlled input can be either shear deformation (Eq. 6.1) or shear stress (Eq. 6.2), and there are many ways to "poke" a material, even with simple shear, including steps and oscillations.

The simplest rheological characteristic of a fluid is the steady shear flow viscosity, defined from steady shear stress τ_{21} and steady shear rate $\dot{\gamma}$ as

$$\eta(\dot{\gamma}) = \tau_{21}(\dot{\gamma})/\dot{\gamma}. \tag{6.3}$$

A Newtonian response would produce constant $\eta(\dot{\gamma})$, but in general it is a function-valued property. This descriptive material function *happens* to be the same function used in the predictive equation known as the generalized Newtonian fluid (see Chap. 1 of this book). But in general, descriptive material functions need not be identical to constitutive model parameters.

Consider the more general possibility of a transient response. For example, a step input of shear rate $\dot{\gamma}(t) = \dot{\gamma}_0 H(t)$ where $H(t)$ is the Heaviside step function. In this case, the transient shear viscosity is defined as

$$\eta^+(t;\dot{\gamma}_0) = \tau_{21}(t;\dot{\gamma}_0)/\dot{\gamma}_0. \tag{6.4}$$

Transient normal stress differences are also used to define material functions, but we will focus on shear stress. A different way to probe the material is to apply a step stress input $\tau_{21}(t) = \tau_0 H(t)$, from which the creep compliance is defined as

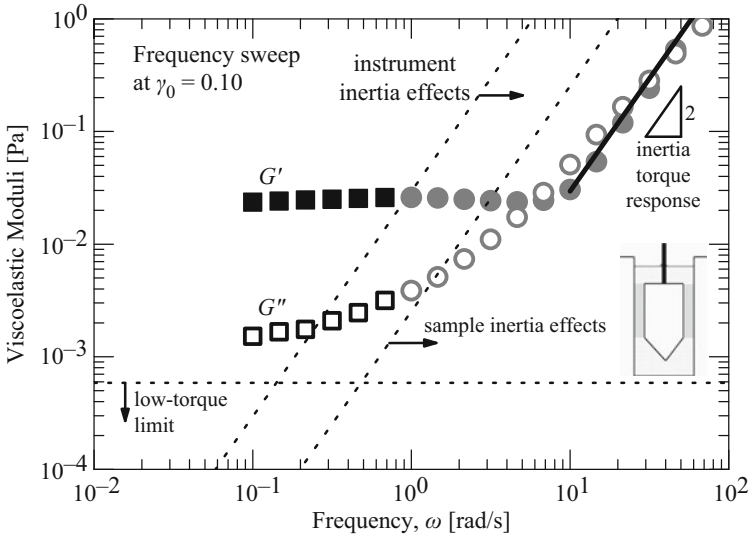

Fig. 6.6 Low-torque and instrument inertia limits shown for oscillatory frequency sweep of hagfish gel. Low-torque limit from Eq. 6.14 with constant γ_0; instrument inertia limit from Eq. 6.18; sample inertia limit from Eq. 6.26. The inertial torque response (*solid line*) is from Eq. 6.20 with $\varepsilon = 0.01$ being the error in the instrument inertia torque correction. *Gray circles* indicate when raw phase angle jumps from $< 15^\circ$ to $> 130^\circ$ which is also an indication that instrument inertia corrections must be made (Data originally published in [5])

$$J(t;\tau_0) = \gamma(t;\tau_0)/\tau_0. \tag{6.5}$$

In this chapter we will also discuss oscillatory inputs [6]. For an input shear rate $\dot{\gamma}(t) = \gamma_0\omega\cos(\omega t)$, the oscillatory shear stress output can be represented by a Fourier series

$$\tau_{21}(t;\omega,\gamma_0) = \sum_n \left\{\tau'_{21,n}(\omega,\gamma_0)\sin n\omega t + \tau''_{21,n}(\omega,\gamma_0)\cos n\omega t\right\}. \tag{6.6}$$

From this, the first harmonic is the most basic feature used to calculate material functions, e.g.,

$$G'_1(\omega,\gamma_0) = \tau'_{21,1}(\omega,\gamma_0)/\gamma_0 \tag{6.7}$$

$$G''_1(\omega,\gamma_0) = \tau''_{21,1}(\omega,\gamma_0)/\gamma_0, \tag{6.8}$$

which are known as the first-harmonic elastic storage and viscous loss moduli, respectively. In the limit of small amplitude oscillatory shear (SAOS), one may expect linear scaling of the stress coefficients with the input amplitude. In this limit of linear viscoelasticity, we need only report the so-called linear viscoelastic storage and loss moduli, $G'(\omega)$ and $G''(\omega)$, respectively.

Shear deformation can be applied with various geometric configurations. We will consider configurations where the stress and strain fields can be calculated without strong assumptions of a particular constitutive model, be it liquid, solid, or nonlinear viscoelastic. For example, indentation tests and embedded particle microrheometry impose nonhomogeneous loading scenarios that change depending on the underlying constitutive model, whereas simplified geometries such as parallel plate, cone and plate and concentric cylinder geometries have well-defined stress and/or strain fields for any material tested (when sample inertia can be neglected; Sect. 3.3), and a constitutive model need not be assumed in order to report the material functions.

Shear stress is the most commonly measured stress component, but normal stresses are also relevant for describing rheological properties in shear. Many of the challenges described here will also apply to normal force measurements, such as experimental windows based on instrument specifications. The reader may find it useful to consult related texts on the topic of rheological measurement for additional details on certain topics [7–9].

3 Challenges

In general, one must keep a system-level perspective to identify bad data and avoid misinterpretations of rheological properties. The following subsections outline particularly problematic sources of error and should serve as a checklist for verifying rheological measurements, especially with soft and slippery biological materials.

3.1 Instrument Specifications

The measurable ranges of load and displacement serve as primary limits to measuring rheological material functions. As shown in Fig. 6.2, the primary measured variables for rotational rheometry include torque T, displacement θ, and rotational velocity Ω. We will use the following notation for conversion factors to calculate stress and deformation

$$\tau_{21} = F_\tau T, \tag{6.9}$$

$$\gamma = F_\gamma \theta, \tag{6.10}$$

$$\dot{\gamma} = F_\gamma \dot{\theta} = F_\gamma \Omega. \tag{6.11}$$

The minimum torque is typically the most important limitation for soft biological systems. Minimum torque is often specified by instrument manufacturers but can often be higher due to other effects (such as surface tension producing torque, Sect. 3.4).

To identify experimental limitations, we will use the approach of drawing boundary lines within the coordinate axes used to report material functions, as done in Fig. 6.3. First, write the reported material functions in terms of the measured quantities and conversion factors. For example, steady shear viscosity from Eq. 6.3 would be

$$\eta(\dot{\gamma}) = \frac{\tau_{21}(\dot{\gamma})}{\dot{\gamma}} = \frac{F_\tau}{F_\gamma}\frac{T(\Omega)}{\Omega}. \tag{6.12}$$

Next, we state the condition for acceptable data that measured torque is above some minimum limit, $T > T_{\text{min}}$. Substituting Eq. 6.12 into the condition $T > T_{\text{min}}$ provides the criteria

$$\eta > \frac{F_\tau T_{\text{min}}}{\dot{\gamma}}, \tag{6.13}$$

for avoiding bad data. This equation was used in Fig. 6.3 for the cone-plate geometry $F_\tau = 3/(2\pi R^3)$ where R is the cone radius and $T_{\text{min}} = 0.1$ μN.m was used.

The appropriate value for T_{min} can sometimes be larger than instrument specification, e.g., with dilute polymers in aqueous solution [10–12]. Recent results show that surface tension torque may be responsible for torque limits higher than instrument specifications [13], as discussed in Sect. 3.4. The limit of minimum measurable viscosity decreases as the shear rate is increased. This is because the limit corresponds to a minimum measurable shear stress $\tau_{21,\text{min}} = F_\tau T_{\text{min}}$, and viscosity is calculated as shear stress divided by shear rate.

A similar downward-sloping low-torque limit appears for other material functions that are plotted as a function of an amplitude. Consider viscoelastic moduli as a function of strain amplitude (Fig. 6.5), for which the low-torque limit sets the minimum measurable viscoelastic moduli

$$G_{\text{min}} = \frac{F_\tau T_{\text{min}}}{\gamma_0}, \tag{6.14}$$

where G_{min} refers to either G' or G''. For the concentric cylinder geometry (single gap) used in Figs. 6.5 and 6.6, $F_\tau = 1/(2\pi R^2 L)$ with minimum torque in oscillation $T_{\text{min}} = 0.003$μN.m as specified by the manufacturer (TA Instruments, AR-G2). In Fig. 6.6, the frequency sweep at fixed strain amplitude, the low-torque limit is simply a horizontal line, since $\gamma_0 =$ constant.

The other primary variable measurements of displacement (θ_{min}, θ_{max}) and velocity (Ω_{min}, Ω_{max}) also provide limits. These can also be plotted as lines within the coordinate axes. In Fig. 6.3 with $\eta(\dot{\gamma})$, the limits (Ω_{min}, Ω_{max}) would appear as vertical lines defining the minimum and maximum $\dot{\gamma}$.

Experimental limits also depend on the geometry choice. This is well known among practitioners. As an example, consider a soft material that may not exceed the minimum measurable torque. Writing Eq. 6.14 more generally, the minimum measurable shear modulus could be written as

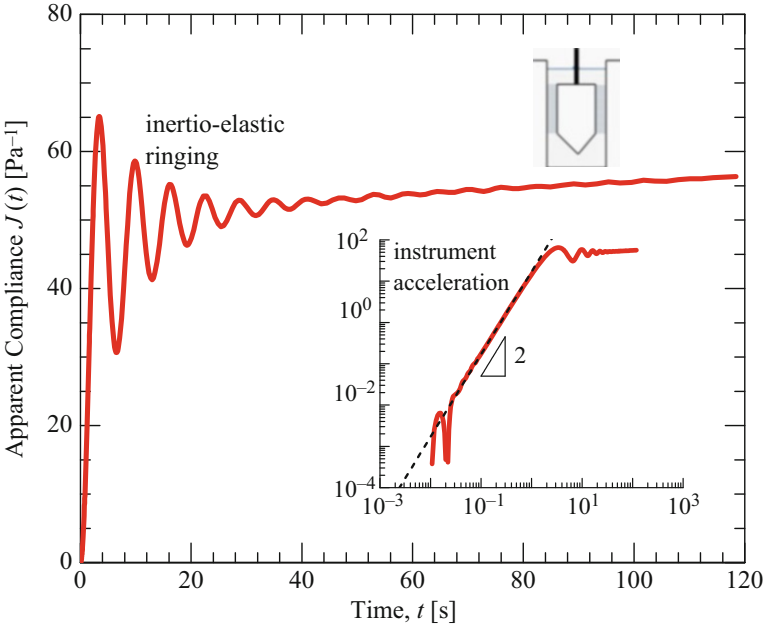

Fig. 6.7 Step torque test with hagfish gel in concentric cylinder geometry. Plotted as apparent compliance $J(t) = F_\gamma \theta(t)/(F_\tau T_0)$, showing instrument inertia effects: acceleration (*inset*) and inertio-elastic ringing. These effects can occur in rheometer designs where load is measured at the moving boundary. The acceleration can be predicted by Eq. 6.23, here using the value $\frac{IF_\tau}{F_\gamma} = 2.9465 \cdot 10^{-2}$ Pa.s^2. The ringing can be used to extract linear and nonlinear viscoelastic information as described in the text. Both effects obscure the true creep compliance of the material (Data originally published in [14])

$$G_{\min} = \frac{F_\tau}{F_\gamma} \frac{T_{\min}}{\theta_{\max}}. \tag{6.15}$$

To measure a very small modulus, one could use a larger displacement amplitude θ_0. However, this may miss the linear viscoelastic regime if the corresponding strain amplitude γ_0 is too large. One can also increase the"gain" in the system that generates the torque from the material resistance. This corresponds to maximizing F_γ/F_τ, e.g., for a cone-plate system $F_\gamma/F_\tau = 2\pi R^3/(3\beta)$, where β is the small cone angle. For a soft material, one may choose a large R to generate sufficient torque to make the measurement or switch to a different geometry with a larger value of F_γ/F_τ, such as concentric cylinders used in Figs. 6.5, 6.6, and 6.7 for the soft hagfish defense gel.

Geometry choices influence other challenges, and there may be trade-offs between different experimental limitations. One issue is inertia of the moving instrument components, if the torque is being measured at the moving boundary. This is outlined in the following section.

3.2 Instrument Inertia

Instrument inertia causes experimental artifacts under *transient conditions*. This includes oscillatory tests (e.g., limiting the high-frequency data in Fig. 6.6) and step tests (e.g., influencing the short-time creep compliance data in Fig. 6.7). This is only a problem if the load is measured at a moving boundary with unsteady motion (as drawn in Fig. 6.1), which is common for many, but not all, commercial rheometers. Unsteady instrument motion involves acceleration, and this requires a load (torque); therefore the measured load is not simply associated with material deformation but also instrument acceleration.

At worst, instrument inertia causes errors that look like real data. Consider yourself warned! For example, the high-frequency data in Fig. 6.6 and short-time data in Fig. 6.7 are not true material properties. In some cases, the effects can be corrected if the instrument inertia is known. At best, the inertial correction is negligible. In still other cases, instrument inertia can cause free oscillations in step load tests. These inertio-elastic free oscillations can actually be used advantageously to characterize material elasticity and dissipation from the ringing frequency and periodic decay, respectively [15–18].

Biomaterials can be exceedingly soft, and instrument inertia artifacts are exaggerated for very soft materials. As examples of softness, the elastic modulus of hagfish gel is $G' \approx 0.2\,\text{Pa}$ (Figs. 6.6 and 6.7), microtubule networks have a plateau modulus $G' \sim 0.4\text{–}20\,\text{Pa}$ [19], vitreous gel $G' \approx 2\,\text{Pa}$ [20], actin networks as low as $G' \approx 1\,\text{Pa}$ [21, 22], fibrin at low concentration $G' \approx 10\,\text{Pa}$ [23], and collagen–hyaluronic acid interpenetrating polymer network hydrogels $G' \approx 1\text{–}100\,\text{Pa}$ [24]. In any soft material, instrument inertia must be carefully considered with transient rheological measurements.

To avoid bad data in oscillatory shear, the "material torque" should exceed the "instrument inertia torque." Thus, the criteria for good data is satisfied under the following condition:

$$T_{\text{material}} > T_{\text{inertia}}, \tag{6.16}$$

$$\frac{G\gamma_0}{F_\tau} > I\theta_0\omega^2, \tag{6.17}$$

$$G > \frac{IF_\tau}{F_\gamma}\omega^2, \tag{6.18}$$

where the variable G represents either G' or G'' in oscillation. Equation 6.18 is used to draw the "instrument inertia" boundary in Fig. 6.6 for the onset of instrument-inertia effects. For the experiment in Fig. 6.6, with a concentric cylinder geometry, $\frac{IF_\tau}{F_\gamma} = 2.9465 \cdot 10^{-2}\,\text{Pa.s}^2$. Equation 6.18 corresponds to the jump in raw phase. Instrument inertia corrections can be made beyond this point, and this requires the subtraction of the instrument inertia torque from the single. This is reasonable to

a point, but artifacts may eventually appear, e.g., with moduli increasing close to $G' \sim G'' \sim \omega^2$. This signature can be explained by inertia effects.

Some of the most prevalent undiagnosed errors in rheometry involve artifacts in high-frequency oscillatory measurements. One should be very careful when interpreting high-frequency data. For example, without drawing the instrument-inertia boundary line in Fig. 6.6, one might be tempted to interpret a curious power-law scaling of viscoelastic properties as a function of frequency. However, this data at high frequency is completely associated with instrument inertia, and not at all a material property.

An instrument inertia artifact at high frequency is most easily diagnosed by looking at the raw phase difference between the oscillating displacement and torque signals and being critical of data points with raw phase $> 90^\circ$. To see why, consider that a purely elastic material response would have load proportional to displacement, $T \sim \theta$, a purely viscous material gives $T \sim \dot{\theta}$, and a purely inertial effect $T \sim \ddot{\theta}$. For time periodic oscillatory signals $T(t)$ and $\theta(t)$, this corresponds to phase differences of 0°, 90°, and 180°, respectively. Without instrument inertia effects, the phase would be limited to the viscoelastic range $0^\circ < \delta < 90^\circ$. So, when this raw phase is $> 90^\circ$, instrument inertia must be playing a role. Corrections can be made by calibrating the rotational inertia and subtracting the expected inertial torque from the total signal (as done for the data in Fig. 6.6). But, this become exceedingly difficult at large values of raw phase when the inertial torque dominates the total torque signal.

Inertia corrections are not 100 % perfect, and this explains the specific signature at high frequency of $G' \sim G'' \sim \omega^2$. One expects inertial torque $T = I\ddot{\theta}$, and for $\theta(t) = \theta_0 \sin(\omega t)$ this is

$$T_0 = I\theta_0\omega^2. \tag{6.19}$$

This can be subtracted from the measured signal, but if the subtraction is not exact, then some of this inertial torque will remain in the processed signal, say εT_0 where ε is (hopefully) a small number. Translated to material properties, this would produce apparent viscoelastic moduli

$$G = \frac{F_\tau(\varepsilon T_0)}{F_\gamma \theta_0} = \varepsilon \frac{F_\tau I}{F_\gamma}\omega^2. \tag{6.20}$$

With $\varepsilon = 0.01$, Eq. 6.20 explains the high-frequency signature in Fig. 6.6. Therefore, even with inertia corrections, viscoelastic moduli will eventually have frequency-dependent power-law scaling that approaches $G' \sim G'' \sim \omega^2$, since they are calculated from a torque signal that is increasingly dominated by inertia and corrections are only precise to within factor of ε.

Instrument inertia affects high-frequency oscillation data, as well as short-time data in step tests. For creep tests (step load input), the instrument inertia can significantly alter the displacement response (Fig. 6.7, hagfish gel). This includes (i) the time required to accelerate and (ii) free oscillations via "inertio-elastic"

ringing, in which the sample elasticity couples with the finite instrument inertia to "ring" at a resonant frequency, just like a mass at the end of a spring [15, 17, 18, 25]. A careful analysis of the inertio-elastic oscillations can reveal both linear and nonlinear viscoelastic properties of the sample [5, 18].

By conservation of momentum, the measured dynamic load must satisfy

$$T(t) = I\ddot{\theta}(t) + \tau_{21}(t)/F_\tau, \tag{6.21}$$

where we have considered a rotational rheometer with instrument inertia I. For a step torque $T(t) = T_0 H(t)$, the initial conditions at $t = 0$ are $\theta = 0$, $\dot{\theta} = 0$, and typically $\tau_{21} = 0$ if starting from rest. Initially, the applied torque is dominated by the acceleration term in Eq. 6.21, since the sample stress term is initially zero and only appears as strain and strain rate increase above zero. The creep response then always has the following form in the limit of short time [17]:

$$\theta(t) = \frac{1}{2}\frac{T_0}{I}t^2 + \cdots. \tag{6.22}$$

Converting this to the apparent material function $J(t)$

$$J(t) = \frac{\gamma(t)}{\tau_0} = \frac{1}{2}\frac{F_\gamma}{F_\tau I}t^2 + \cdots \tag{6.23}$$

which shows the general short-time instrument acceleration artifact, independent of applied torque when plotted as apparent compliance $J(t)$. This is shown in the inset of Fig. 6.7 for the soft hagfish gel.

Inertio-elastic ringing analysis can probe both linear viscoelasticity [15, 17] and nonlinear viscoelasticity [5, 18] in novel ways. Such analysis requires the assumption of an underlying constitutive model for $\tau_{21}(t)$ in Eq. 6.21, e.g., a three-element fluid (Jeffreys), or two-element solid (Kelvin–Voigt). Detailed calculations associated with the inertio-elastic ringing analysis can be found in the references above.

To avoid the instrument inertia effects discussed in this section, one can measure the load (torque) at the *stationary* boundary, e.g., with a force rebalancing transducer, rather than measuring load at the moving boundary, e.g., through a motor. This requires more complex instrumentation to separate the imposed displacement from the measured load, but such separated motor-transducer instruments are commercially available. These setups can eliminate important errors due to instrument inertia including the accurate measurement of stress jumps in response to step displacement inputs [26].

3.3 Fluid Inertia and Secondary Flows

Even if instrument inertia is eliminated, the sample itself will always have finite inertia which can produce artifacts from momentum diffusion, viscoelastic waves, and secondary flows, all of which can violate the assumption of homogeneous simple shear deformation in Eq. 6.1. Purely elastic instability can also produce secondary flows even in the limit of vanishing Reynolds number [27–30]. This section will discuss the symptoms of both wave propagation and secondary flows and how to identify experimental limits due to these artifacts.

3.3.1 Wave Propagation at High Frequencies and Short Timescales

The assumption of homogeneous simple shear strain is violated when there are waves propagating through the material. Propagating waves may come from either viscous momentum diffusion or elastic shear waves or both for viscoelastic materials in general.

The general criteria for approximately homogeneous strain in the velocity gradient direction is that the wavelength l of any propagating wave should be much larger than the geometry gap D

$$l \gg D \tag{6.24}$$

so that, in the gap region, the velocity field is negligibly affected by the propagating wave [31]. Two key questions must be answered: (i) how much smaller must the gap D be for tolerable errors, and (ii) how can the wavelength l be calculated? The wavelength l depends on material properties and the frequency (time scale) of motion. Most importantly, l decreases with high driving frequency, and we therefore expect wave propagation issues at high frequency and short time scales.

Schrag gave a detailed analysis of linear viscoelastic wave propagation [31], showing that linear viscoelastic shear waves between a moving boundary and a fixed reflecting boundary have wavelength

$$l = \frac{1}{\cos(\delta/2)} \left(\frac{|G^*|}{\rho} \right)^{1/2} \frac{2\pi}{\omega}, \tag{6.25}$$

where ω is the driving frequency, $|G^*| = \sqrt{G'^2 + G''^2}$ is the magnitude of the complex modulus, δ is the viscoelastic phase angle, and ρ is the fluid density. The scaling in Eq. 6.25 is $l \sim c\mathscr{T}$ where c is the wavespeed $c \sim (|G^*|/\rho)^{1/2}$ and $\mathscr{T} = 2\pi/\omega$ is the wave period. Using the criteria $l \geq 10D$ to avoid errors of possibly 10 % [31], along with Eq. 6.25, we can identify an approximate edge of the experimental window for plots of viscoelastic moduli,

$$|G^*| > \left(\frac{10}{2\pi} \right)^2 \cos^2(\delta/2) \rho \omega^2 D^2, \tag{6.26}$$

which is used in Fig. 6.6 to identify the "sample inertia limit," using a value $\cos^2(\frac{\delta}{2}) = 1$. Equation 6.26 scales as $|G^*| \sim \rho\omega^2 D^2$, showing the important sensitivity to both driving frequency ω and geometry gap D. Higher frequencies are problematic. Smaller gas are helpful. The numerical front factor has weak dependence on δ, since $\frac{1}{2} < \cos^2(\frac{\delta}{2}) < 1$. The more sensitive number is the factor by which $l > D$. More precise experiments require a larger separation of these lengthscales, as detailed in Schrag [31] (his Table 1). Whatever the front factor, the shape of the experimental limit will still be the same, scaling as $|G^*| \sim \rho\omega^2 D^2$. The sample inertia impacts measurement at high frequency and low modulus, and therefore soft gels and low-viscosity fluids will have greater propensity for sample inertia effects.

Although strain amplitude does not appear explicitly in Eq. 6.26, fluid inertia problems can appear due to large-amplitude oscillations [32], even with constant forcing frequency. For these nonlinear tests, one can conceptually think about $|G^*|$ changing in the nonlinear regime, which would influence the wave propagation speed and therefore the wavelength l. When large-amplitude oscillatory shear strain softens a sample (decreasing $|G^*|$ which is typical for polymer melts), then the sample inertia issue will become more problematic at large strain amplitudes. This is consistent with detailed studies in the literature on flexible polymers [32]. However, if a sample becomes more stiff in the nonlinear regime (increasing $|G^*|$ which is typical of semiflexible biopolymer gels [33]), then one could argue that the inertia artifact may actually be less problematic due to increasing viscoelastic wavelength l. This possibility, however, has not yet been studied in any detail. One challenge for universal analysis of nonlinear viscoelastic measurements with wave propagation is that no universal constitutive equation exists for nonlinear viscoelasticity.

The experimental boundary line defined by Eq. 6.26 should serve as a general guideline to identify possible experimental windows due to shear waves when measuring oscillatory shear material functions. It is useful in linear viscoelastic plots, e.g., $G'(\omega)$,$G''(\omega)$ (as in Fig. 6.6), and may also be useful to estimate the boundary for nonlinear tests, e.g., large-amplitude oscillatory shear (LAOS) tests in terms of $|G_1^*|(\gamma_0)$. For all these cases, the artifact of viscoelastic waves will limit measurement of low modulus and high-frequency data.

3.3.2 Secondary Flows at High Velocity

Sample inertia can also cause nonideal velocity fields during *steady* flow. Even before turbulent flow, high velocities can cause secondary flows superposed on the primary simple shear flow due to finite sample inertia and curved streamlines in unstable configurations. This includes cylindrical geometries with a rotating inner cylinder and planar geometries including cone-plate and parallel disk flow. In each case, secondary flow increases the measured torque and therefore incorrectly increases the apparent viscosity of the fluid. For example, a Newtonian fluid with secondary flow present would incorrectly appear as shear thickening, since the secondary flow effects grow with increasing velocity. This is observed in Fig. 6.3 with the microalgae suspension at high shear rates.

Concentric cylinder measurements have a well-known secondary flow instability that appears when the inner cylinder is rotating at sufficiently large velocity Ω. Known as Taylor–Couette flow after the initial work of Taylor [34], the inertial instability causes axisymmetric vortices. The stability criteria is well established for Newtonian fluids in the limit of small gaps. It is based on a sufficiently small Taylor number Ta [35,36]:

$$\mathrm{Ta} = \frac{\rho^2 \Omega^2 (R_o - R_i)^3 R_i}{\eta^2} < 1{,}700, \tag{6.27}$$

where R_i is the inner radius moving at angular velocity Ω and R_o is the fixed outer radius. The criteria has been mapped for corotating and counterrotating cylinders as well [88], but the most useful criterion for standard shear rheometry is given in Eq. 6.27. There is some evidence that non-Newtonian polymer solutions increase the critical Taylor number, so that Eq. 6.27 is a conservative estimate for experimental rheological measurements [8]. To draw an experimental boundary line on a plot of viscosity versus shear rate $\eta(\dot{\gamma})$, rearrange Eq. 6.27 and use the definition of shear rate $\dot{\gamma} = \Omega R_i/(R_o - R_i)$. This gives the condition

$$\eta > \frac{(R_o - R_i)^{5/2}}{1{,}700 R_i^{1/2}} \rho \dot{\gamma} \tag{6.28}$$

to avoid Taylor vortices. The criteria emphasizes that low-viscosity fluids are more prone to this secondary flow and that small gaps are very helpful in the geometry design. The scaling $\eta \sim \dot{\gamma}$ defines the shape of the boundary on a plot of $\eta(\dot{\gamma})$ and limits high shear rate measurements. As a quantitative example of an experimental limit for the concentric cylinder geometry, consider properties typical of biological fluids, density $\rho = 10^3$ kg/m^3, and viscosity near water $\eta = 1$ mPa.s. For a nominal concentric cylinder geometry with gap $(R_o - R_i) = 1$ mm and inner radius $R_i = 11.8$ mm (based on the ISO 3219 standard with $R_o/R_i = 1.0847$ [37]), Eq. 6.28 can be rearranged to show the shear rate is limited to $\dot{\gamma} < 5.8 \cdot 10^3\ \mathrm{s}^{-1}$. This is reasonably high, but of course will change depending on the actual viscosity and size of geometry being used.

Cone-plate and parallel disk geometries have a secondary flow that is always present at finite rotational velocity [38] (the critical Taylor number does not apply to these geometries). Here, centrifugal effects create a radial velocity component with outward flow at the rotating boundary. Due to conservation of mass this causes inward flow at the stationary boundary. (Highly elastic liquids can change this scenario as discussed in the following section.) For the Newtonian case, the strength of the flow is based on a Reynolds number. The secondary flow increases the measured torque, and this can be used to set a criteria and draw experimental limits for measurement. For Newtonian fluids with cone-plate or parallel disk geometry, the measured torque T is predicted to depend on the Reynolds number as [39]

$$\frac{T}{T_0} = 1 + \frac{3}{4{,}900}\mathrm{Re}^2, \tag{6.29}$$

where T_0 is the ideal torque due to shear flow alone and Re is the Reynolds number defined as

$$\mathrm{Re} = \frac{\rho \Omega L^2}{\eta_0}, \tag{6.30}$$

where L is the representative gap lengthscale. For cone-plate, $L = \beta R$ where β is the angle between the cone and plate, and for a parallel plate, $L = H$ where H is the gap. For a given error bound on T/T_0, we can identify a critical Reynolds number $\mathrm{Re}_{\mathrm{crit}}$. For example with 1 % error, i.e., $T/T_0 = 1.01$, the critical Reynolds number is $\mathrm{Re}_{\mathrm{crit}} = 4$. This clearly occurs before turbulence could be sustained [38], and therefore sets the experimental boundary for rheological measurements. Using the criteria $\mathrm{Re} < \mathrm{Re}_{\mathrm{crit}}$ and the definition of shear rate $\dot{\gamma} = \Omega R/L$, results in an experimental limit that can be shown on plots of steady shear viscosity $\eta(\dot{\gamma})$,

$$\eta > \frac{L^3/R}{\mathrm{Re}_{\mathrm{crit}}}\rho\dot{\gamma} \tag{6.31}$$

which is used in Fig. 6.3 to draw the "secondary flow limit" line, using $\mathrm{Re}_{\mathrm{crit}} = 4$ and $L = \beta R$ for the cone-plate geometry. Figure 6.3 also shows the expected apparent shear thickening of the shear viscosity, based on Eq. 6.29, and converting to apparent viscosity. Equation 6.31 shows the scaling $\eta \sim \rho\dot{\gamma}$, similar to the shape of the boundary with concentric cylinders and the Taylor–Couette instability, Eq. 6.28.

In all the rotational geometries discussed here, lower viscosity fluids have a smaller experimental window with limitations at high shear rate due to secondary flow.

3.3.3 Purely Elastic Instabilities

Undesirable secondary flows can also be created by purely elastic instabilities, in the limit of vanishingly small Reynolds number. These secondary flows arise from a different physical effect than the previous subsection (i.e., not fluid inertia). For purely elastic instabilities, curved streamlines carrying tension cause instability [27–30]. The effect occurs at high Weissenberg number $\mathrm{Wi} = \lambda_1\dot{\gamma}$ (where λ_1 is the longest relaxation time of the fluid) for elastic liquids in rotational geometries including concentric cylinder, cone-plate, and parallel disk.

The primary symptom of secondary flow is increased torque. Hence, the apparent steady-state viscosity may incorrectly appear to shear thicken (Fig. 6.8). Increased normal force may also occur. The purely elastic secondary flow occurs at a critical Wi which depends on the measurement gap and constitutive behavior of the fluid. Specific predictions are available for certain models including upper-convected

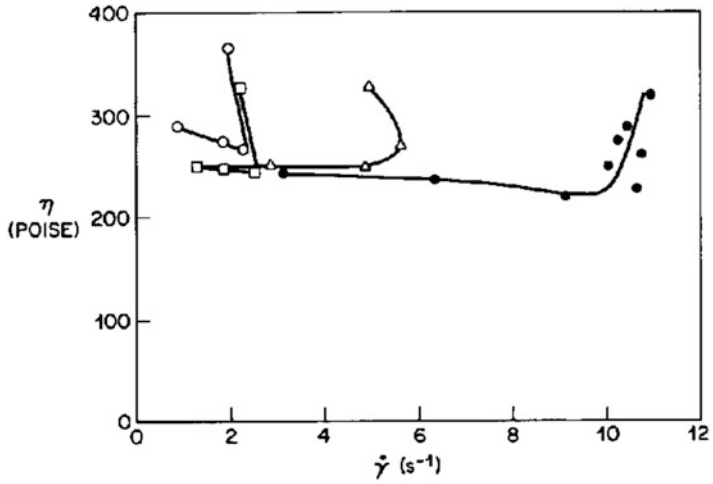

Fig. 6.8 Purely elastic instabilities cause apparent shear thickening of steady shear viscosity. Here with a dilute solution of polyisobutylene with nominal molecular weight $2.7 \cdot 10^6$ from [27]. The thickening appears at a critical shear rate (Weissenberg number); the accessible range of experiments is extended by decreasing the gap, here with a parallel disk geometry at different gaps ranging from 2 mm (*open circles*) to 0.3 mm (*filled circles*). (Reprinted from Magda and Larson [27], Journal of Non-Newtonian Fluid Mechanics, Fig. 10, Copyright (1988), with permission from Elsevier)

Maxwell and Oldroyd-B [28, 29]. Smaller geometry gaps inhibit the instability, pushing the critical shear rate higher as shown in Fig. 6.8. Very large solvent viscosity can also inhibit the instability. The effect is time-dependent, appearing after prolonged shearing [27]. A general instability criteria applicable to complex geometries has been suggested which includes dependence on both Weissenberg and Deborah numbers [29,30]. Purely elastic instabilities in pressure-driven channel flow have also been described [40, 41].

For elastic instabilities to occur before the fluid inertia instabilities (Sect. 3.3.2), the fluid must have a long relaxation time so that the Weissenberg number can be large while Reynolds number or Taylor number is low. For polymeric systems including biological fluids, elastic instabilities are relevant with high-molecular-weight polymers in solution.

For all secondary flows, due to either fluid inertia (Sect. 3.3.2) or fluid elasticity (this subsection), the symptoms are similar: increased viscosity at high shear rates, as seen in Figs. 6.3 and 6.8. These effects limit the high shear rate experimental range for measuring simple shear rheological properties, and tempt misinterpretation of apparent shear thickening at high rates.

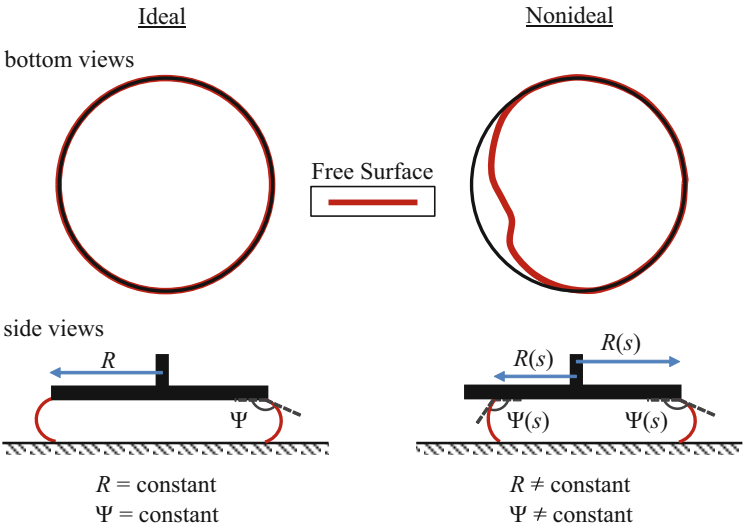

Fig. 6.9 Contact line and interface angle: ideal versus nonideal. Nonideal asymmetries are exaggerated compared to typical loading and can also occur as a result of overfilling. The nonideal condition may create artifacts of apparent shear thinning due to the presence of a constant surface tension torque (Figure adapted from [13])

3.4 Surface Tension Forces

For rotational rheometers, surface tension results in a torque that should not occur in an ideal, rotationally symmetric geometry [13] (Fig. 6.9). It is typically neglected, but the phenomenon may exceed the instrument low-torque limit $T_{\min}$ by orders of magnitude. The effect causes Newtonian fluids, including water, to appear as shear thinning with finite elastic modulus (Figs. 6.10 and 6.11). We discuss the symptoms of the effect, methods for drawing experimental boundaries with a different $T_{\min}$, and techniques to minimize the effect, which is particularly important when measuring aqueous solutions such as biological fluids.

In this section, the focus is rotational geometries where surface tension influences the measurement of shear stress. This is a significant experimental challenge for measuring soft, active, or low-viscosity biological fluids. Related issues not discussed here include (i) normal force from surface tension [42, 43] which is highly dependent on meniscus shape [44–46]; (ii) sliding plate instruments which dilate free surface area and cause surface tension artifacts in shear stress calculations [47–49]; and (iii) surface rheology artifacts from films of surface-active components [50, 51] which will be discussed in Sect. 3.5.

Surface tension torque is caused by traction forces around a material contact line that has broken rotational symmetry, both in terms of geometric location and non-constant contacting angle (or nonconstant surface tension) [13] (Fig. 6.9).

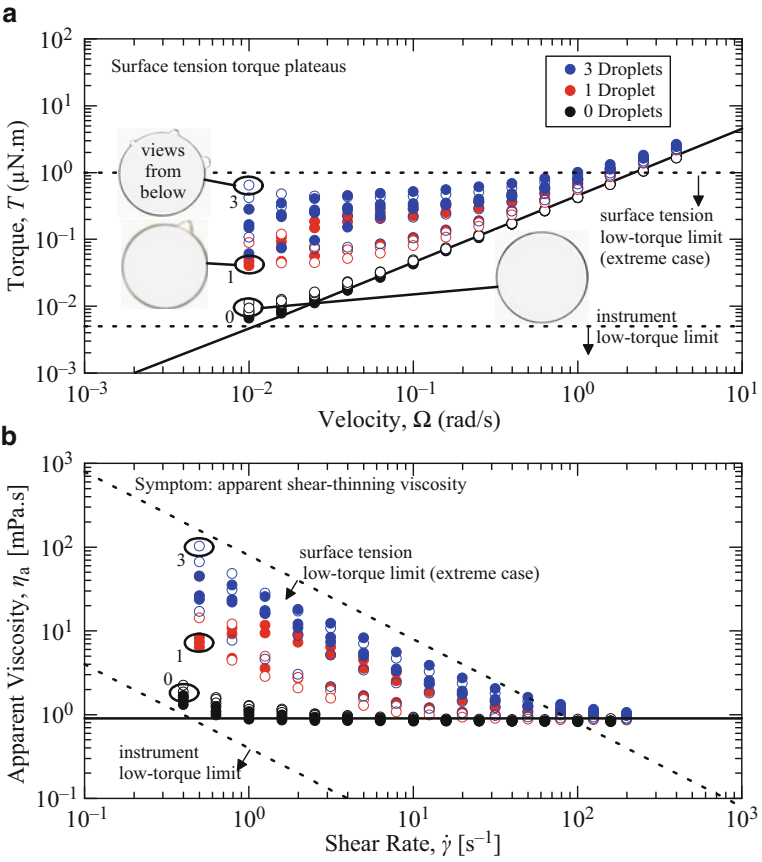

Fig. 6.10 Surface tension can generate torque in *steady* shear (**a**), which could be mistaken as shear thinning (**b**), as shown here with water at room temperature. The effect grows with slight overfilling that increases contact line rotational asymmetry, here with 1 or 3 small extra droplets of water at the boundary, yet the effect can be present even with best practices ("0 droplets") where residual torque plateaus appear above the instrument low-torque limit. Views from below in (**a**) indicate droplet contact lines around the $D = 40$ mm plate, as viewed through a glass bottom plate. Low-torque limits for $\eta_{\min}$ drawn from Eq. 6.13 using $T_{\min} = 5$ nN.m (instrument low torque) and $T_{\min} = 1\,\mu$N.m (surface tension torque, extreme case) (Figure adapted from [13])

Historically, rotational symmetry has been a primary assumption [2, 8], even when considering effects of surface tension [42, 43]. However, the rotational symmetry assumption can be violated easily. Finite deviations of contact line rotational symmetry, from manufacturing tolerances or sample overfill/underfill, allow surface tension to produce a torque which may dramatically impact measurements of shear rheology, particularly at low shear rates and for low-viscosity fluids.

Symptoms of surface tension torque include apparent viscous shear thinning and elastic shear modulus. In steady shear flow, the effect appears as a superposed constant torque independent of rate (Fig. 6.10a). These torque plateaus would appear

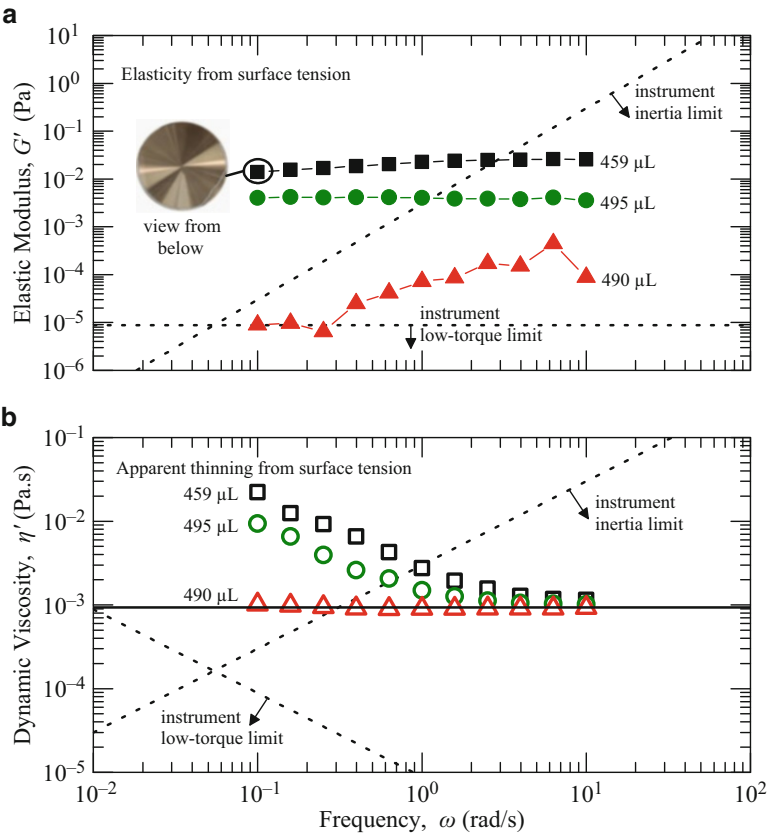

Fig. 6.11 Surface tension can generate torque in *oscillatory* shear, which could be mistaken as shear elasticity (**a**) and nonconstant dynamic viscosity (**b**), as shown here with water at room temperature. Slight underfill or overfill can break contact line rotational symmetry (sample volume 459–495 µL for a $D = 60$ mm steel cone), as shown in the *inset* view from below at 459 µL. Oscillatory strain amplitude $\gamma_0 = 100\,\%$. Instrument low-torque limit for G'_{min} and η'_{min} from Eq. 6.14 with $T_{\text{min}} = 0.5$ nN.m in oscillation and instrument inertia limit for G'_{min} and η'_{min} from Eq. 6.18 using $\frac{IF_\tau}{F_\gamma} = 3 \cdot 10^{-3}$ Pa.s^2 (Figure adapted from [13])

inaccurately as apparent shear thinning of water (Fig. 6.10b). This example shows the dramatic impact of slight overfill that breaks the rotational symmetry of the contact line. The impact is to raise the effective T_{min} in the low-torque limit for $\eta(\dot{\gamma})$, based on Eq. 6.13. This may help explain studies showing a practical low-torque limit 20 times larger than that stated by the equipment manufacturer [10–12].

In oscillatory measurements, surface tension artifacts can mistakenly appear as a storage modulus G' plateau. We see this for water in Fig. 6.11a. Figure 6.11b also demonstrates frequency-dependent dynamic viscosity η', which should be constant for water over this range of frequencies. The inset image shows the asymmetric contact line for a slightly underfilled sample. When the geometry is visually

properly filled (to within 5 μL, red triangles in Fig. 6.11), the elastic modulus is unmeasurable to within the experimental limits of low torque and instrument inertia, and the proper dynamic viscosity η' is measured down to $\omega = 10^{-1}$ rad/s.

The examples of Figs. 6.10 and 6.11 show that the surface tension torque effect is highly variable due to sample loading, wetting conditions, and contact line asymmetries and cannot be deterministically corrected in experimental measurements. It therefore raises the lower bound of the instrument low-torque limit T_{min}, in some cases by orders of magnitude.

Experimental techniques and careful geometry selection must be used to minimize surface tension effects. The surface tension torque is reduced by maximizing rotational symmetry of the contact line, minimizing evaporation and the migration of the contact line, reducing the radial location of the contact line, and lowering the surface tension. Experimental techniques for controlling the contact line symmetry such as using matched plate geometries are helpful. Reducing evaporation with a solvent trap and precision sample loading with a micropipette can also minimize surface tension torque plateaus.

Identifying and eliminating the surface tension torque is critical for low viscosities, intrinsic viscosities, soft materials, subdominant viscoelastic components, small gaps, and any circumstance where the low-torque limit is experimentally important. This phenomenon should be especially important in aqueous systems, including biological fluids, due to the high surface tension of water.

3.5 Free Surface Films

Biological fluids may contain proteins and other components that are surface active. Such components have an affinity to accumulate at liquid-air interfaces and may create a rigid or semirigid surface film. The film itself can be a fascinating object of study (e.g., see Chap. 4 of this book), but the film formation is a problem when the bulk flow properties of the solution are of interest. This experimental challenge has been known for some time [8, 50]. Care must be taken when measuring rheology using a geometry that involves a free surface, otherwise fluids may appear non-Newtonian when they are not measurably so [50, 51]. This applies to all the rotational geometries discussed in this chapter.

The primary signatures of a free surface film include increased viscosity, enhanced shear thinning, and often the presence of an apparent yield stress. For example, this is shown in Fig. 6.12 for aqueous solutions of the protein bovine serum albumin (BSA) [51]. The figure compares measurements using a cone-plate geometry (with liquid-air interface) and a microchannel pressure-driven flow viscometer (internal flow without a liquid-air interface). The microchannel measurements suggest Newtonian viscosities for this range of protein concentrations and shear rates, and do not match the cone-plate measurements which show higher viscosities and shear thinning at low rates. The increased viscosity and shear thinning are caused by a free surface film of the BSA [51]. A film is undesirable

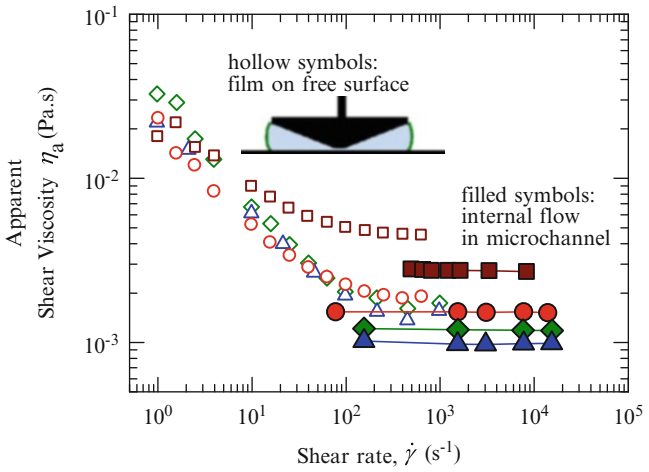

Fig. 6.12 Surface-active components in solution, such as the protein bovine serum albumin (BSA) shown here, may form a film at a free interface. Such films can show apparent yield stress and shear thinning of the apparent bulk viscosity when tested with cone-plate (*hollow symbols*). However, this is an interfacial rheological property and not a true bulk property as shown by the internal channel flow measurements (*filled symbols*). BSA at bulk concentrations of 10–200 mg/mL, *triangles-squares* (Data originally reported by Sharma et al. [51])

when measuring bulk properties. Of course, the presence of a film does provide an opportunity for interfacial surface rheology measurements if this is desired.

Internal flow geometries and guard rings (which eliminate the interface) can avoid the problem (although even in a closed system, there is the possibility of biofilm formation in biological fluids). When these are not available or possible, then one must be mindful of the symptoms of a free surface film. To test for the artifact of surface film rheology, one could make repeated measurements with different geometries and check for reproducibility of apparent material functions. For example, cones with increasing diameters could be used. The larger diameters create a longer film length and larger moment arm to produce torque and would generally be expected to have increased torque effects due to free surface films.

3.6 Slip

In rheological characterization, it is typically assumed that the sample sticks to the contacting boundaries whose motion defines the assumed strain field. In fluids, this is known as the no-slip condition. However, slip can easily occur [52–54], especially with biological gels and tissues. Slip violates the assumptions of standard

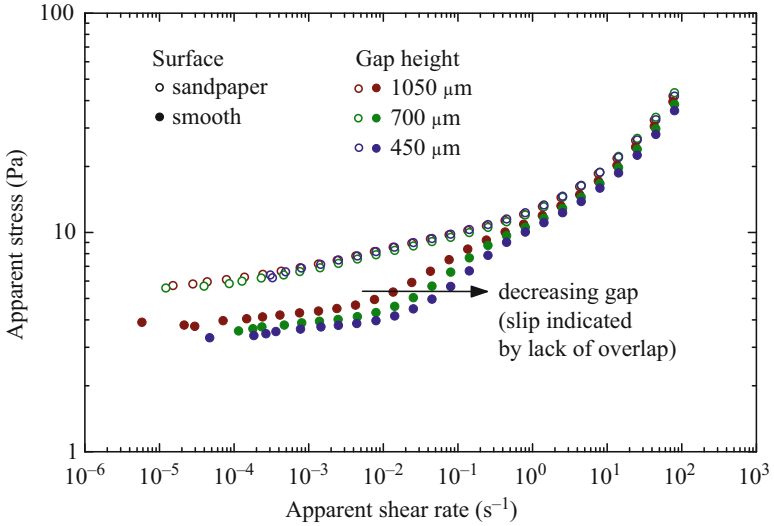

Fig. 6.13 Slip behavior on a smooth geometry surface can decrease flow stress and cause inconsistent gap dependence, as shown here for Nivea Lotion tested with different surfaces and gaps using parallel disks of diameter $D = 40$ mm. A sandpaper surface eliminates slip artifacts, showing superposed data for different gap heights (Previously unpublished work of author RHE)

rheological characterization and may cause significant artifacts in the data. This section describes slip artifacts, methods of checking for slip, and techniques for avoiding the problem altogether.

The key signatures of slip include a decreased flow stress and inconsistent apparent stress and strain rate that depend on the geometry gap (gap height with parallel disks or cone angle with cone-plate). Figure 6.13 demonstrates these slip artifacts as seen with a non-Newtonian fluid (Nivea Lotion). The smooth boundary geometry produces artifacts and the true material behavior can be seen with a roughened surface. The steady-state flow sweep is conducted from high to low rates using a combined motor-transducer rotational rheometer (AR-G2, TA Instruments) with a parallel disk of diameter $D = 40$ mm and controlling temperature to $T = 23\,^{\circ}\mathrm{C}$ with a Peltier plate. The sandpaper surfaces are adhesive-back sandpaper, 600 grit (McMaster-Carr Part #47185A51) attached to the standard rheometer geometry on both bounding surfaces. Apparent shear stress is calculated as $\tau_a = F_\tau T$ with $F_\tau = 2/(\pi R^3)$ for the disk, and apparent shear rate from $\dot{\gamma}_a = \Omega/h$ where h is the geometry gap.

Figure 6.13 shows an apparent stress plateau at low rates (an apparent dynamic yield stress) that depends on the geometry being used. The smooth geometry shows a lower apparent yield stress. This is a common experimental artifact that has been discussed in the literature, especially with yield stress fluids [55, 56]. In a recent study with a dense colloidal system, apparent yield stress behavior at low rates was associated with a sub-colloidal lubrication layer at the wall, as confirmed by confocal microscopy [56].

The gap is varied to check for slip in Fig. 6.13. For the rough sandpaper surface, the measurements superpose for all gaps therefore confirming the absence of slip. However, for the smooth plate, the data shifts to higher apparent strain rate as the gap is decreased. This shift is important evidence to indicate slip. To understand why, consider the simple example where an applied stress results in a particular slip velocity at the boundary of a sample. The gap-independent slip velocity contributes a fixed amount to the total velocity Ω. Therefore, as the gap h decreases, the apparent shear rate $\dot{\gamma}_a = \frac{\Omega R}{h}$ will have a numerator that decreases slower than the denominator, therefore increasing $\dot{\gamma}_a$ at small gaps for a fixed stress. This is shown by the arrow in Fig. 6.13 pointing to the right. Varying the geometry checks for the presence of slip but can also be used to correct for slip [57]. With very good control and sensitive instruments, gap-dependent measurements with a linear sliding plate rheometer have been used to characterize the slip itself including slip velocities [58].

Although sandpaper may be sufficient for some biological gels, e.g., as used for biopolymer mucin gels (snail slime) [59], sandpaper roughness is not always sufficient and other techniques must be considered. This includes the addition of grooves [55] or "cleats" [60] in plates, e.g., as used to measure vitreous humor [61]. Vane rotors are also commonly available [62], which are modifications of the concentric cylinder geometry. For more challenging solid materials, such as soft biological tissues, the sample can be squeezed slightly with an applied normal load to prevent slip during shear tests [63]. In extreme cases, gluing the tissue to the plate is required, as shown to be important with porcine kidney tissue, especially in nonlinear tests [64].

3.7 Small Volume and Small Gap

Biological fluids may be available only in small quantities. A variety of techniques can be used for measurements on small sample volumes [49]. This section describes a few techniques that have been useful with biological fluids and then focuses on the most widely accessible technique: parallel disks at small gaps. This section then describes the artifacts, corrections, and experimental windows for measurements at small gap.

Several techniques have been used for sample volumes around 10 µL and below. An early example is a capillary rheometer apparatus requiring only about 10 µL in volume [65]. A more recent pressure-driven flow setup (microfluidic cross-slot extensional flow) requires approximately 1 µL volumes [66], as demonstrated with hyaluronic acid and saliva. Boundary-driven flow examples include modification of parallel disks to confine a sample near the outer radius over a small area, approximating sliding plate flow with volumes 1–25 µL [48]. A custom-built linear sliding plate instrument has also been developed for precise, small gap tests (the so-called flexure-based microgap rheometer (FMR) [67, 68]). The FMR has been used to measure microliter quantities of spider silk [69] and sub-microliter quantities of carnivorous plant mucilage [70]. In those studies, samples were also tested with a small-scale extensional instrument based on capillary breakup extensional

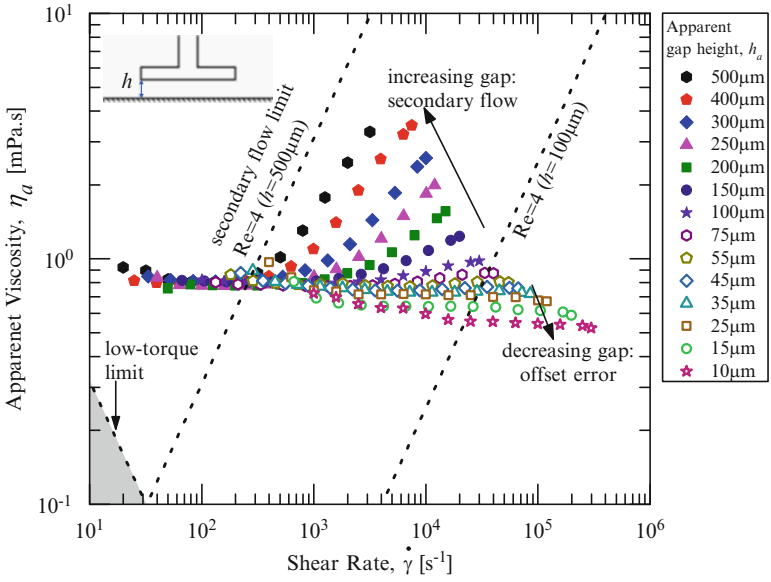

Fig. 6.14 Small gap/volume measurements of water with plate geometry, $D = 20$ mm. Gap offset artifacts are seen for apparent gap heights $h_a < 50$ μm. Inertial secondary flow artifacts appear for sufficiently large Reynolds number, i.e., at larger gaps and high shear rate (Sect. 3.3) (Previously unpublished work of authors RHE and MTJ)

rheometry (CaBER). Embedded probe techniques are also useful. Nanoliter droplets of butterfly saliva have been characterized with an embedded magnetic rod [71]. Of all the demonstrated techniques, standard parallel disks at small gaps may be the most experimentally accessible option for a researcher interested in small volumes of biological fluid.

With parallel disks, the smallest accessible gap will be limited by disk parallelism, precise knowledge of the true gap, and the size of the underlying material structure in the fluid. Confinement effects that violate the continuum hypothesis will not be discussed here (although this is sometimes relevant in biological fluids, such as blood exhibiting a confinement-dependent viscosity [72]). Finite boundary roughness and tribological contact will not be discussed either, since other gap errors are typically encountered first. Gap errors, including parallelism and gap precision, are the primary concern, assuming the continuum hypothesis holds true.

For gap errors, measurement artifacts include a decreasing apparent viscosity at smaller gaps (Fig. 6.14). This occurs under the typical scenario where the true gap h is larger than the apparent gap h_a calibrated by apparent contact of the plates [73]. These symptoms and limitations apply similarly to any boundary-driven drag flow at small gaps, such as the sliding plate FMR [67] and techniques to isolate samples to a small region under a conventional parallel disk geometry [48], although the difference between h and h_a may change depending on the calibration procedure.

Figure 6.14 shows the expected artifacts for small gap measurements, here with water using a disk with diameter $D = 20\,\text{mm}$ down to apparent gap $h_a = 10\ \mu\text{m}$ (down to apparent volume around $3\,\mu\text{L}$). Using small gaps requires less volume and allows for higher shear rates. On average, the viscosity is what we expect for water, $\eta \approx 1$ mPa.s, but there are some issues. For small gaps ($h_a < 50\ \mu\text{m}$), the apparent viscosity decreases as a function of gap. For the larger gaps ($h_a \geq 100\ \mu\text{m}$), the viscosity seems to shear thicken at high shear rates, but at different critical shear rates. These are not true material properties of water, but are artifacts that can be explained.

For larger gaps at high rates, the inertia of the liquid may cause secondary flows (as described in Sect. 3.3). It is common to assume that the liquids will travel in circular stream lines, but centrifugal effects will tend to push fluid outward near a rotating boundary. This secondary flow increases dissipation, resulting in higher measured torque and hence a larger apparent viscosity. The effect increases as a function of Reynolds number, defined as $\text{Re} = \rho\Omega h^2/\eta$, so the effect is evident for higher velocity Ω, larger gaps h, and low-viscosity fluids. Lines for $\text{Re} = 4$ are shown in the figure for two representative gap heights.

For small gaps, the main error is caused by a gap offset ε_h, which is the difference between the apparent calibrated gap h_a and true gap h [73],

$$h = h_a + \varepsilon_h. \tag{6.32}$$

(The term "true" gap means the "effective" or "average" gap since the disks have finite roughness and finite parallelism manufacturing tolerance. Hence the gap is not precisely constant throughout the test geometry.) Since apparent gap h_a is used to calculate apparent viscosity η_a, one expects deviation from the true viscosity to be of the form

$$\eta_a = \eta \frac{h_a}{h} \tag{6.33}$$

which indicates $\eta_a < \eta$ for offset $\varepsilon_h > 0$. The apparent gap h_a is typically calibrated based on contact force at the first point of contact, where h_a is set to zero. Two issues arise to create gap offset error $\varepsilon_h > 0$. (i) A finite force is often observed before solid–solid contact due to viscous resistance of air flow in the squeezing gap. (ii) The parallelism is not perfect, and the average gap will often be larger than the "first point of contact" gap. The nonparallelism contribution generates normal forces [74] and this can be used to identify the relative importance of the two sources of gap offset error. Both of these effects contribute to gap offset error $\varepsilon_h > 0$, so that the actual gap is larger than the apparent value. Typical values for ε_h are on the order of 10–50 μm [75, 76].

Gap offset ε_h can be corrected if Eq. 6.32 holds true [73, 75, 76], although the correction will depend on the uncertainty in calibrating for ε_h. Uncertainly in the calculated viscosity will grow dramatically as the gap approaches the uncertainty of ε_h. Gap offset errors can be minimized by using a smaller radius plate, since

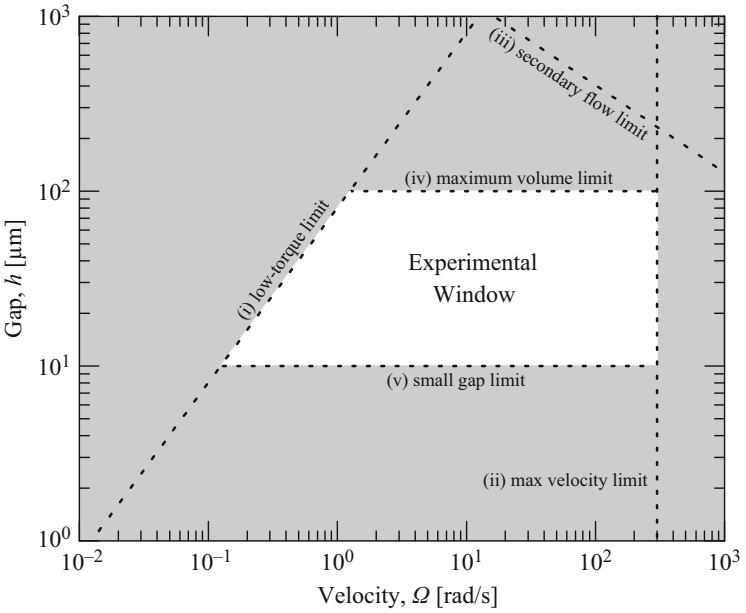

Fig. 6.15 Experimental window for small volume aqueous solutions, using Eqs. 6.34–6.38 to draw the boundaries. Representative values used are $T_{\min} = 5$ nN.m, $\Omega_{\max} = 300$ rad/s, $\mathrm{Re}_{\max} = 4$, $\eta = 1$ mPa.s, $\rho = 1{,}000$ kg/m^3, plate diameter $D = 8$ mm, $V_{\max} = 5\,\mu$L, and minimum gap $h_{\min} = 10\,\mu$m

this decreases the viscous squeeze force at apparent contact and also decreases the nonparallelism (angular misalignment) contribution to ε_h due to the smaller radius. However, a smaller radius plate changes other experimental limits such as increasing $\eta_{\min}$ due to the low-torque limit (Eq. 6.13). The experimental window for small gap measurements is therefore bounded by several limitations.

Figure 6.15 is an example experimental window for small volume and small gap measurements, in the operational space of gap h and velocity Ω. Several limitations are considered including (i) minimum torque, (ii) maximum velocity, (iii) secondary flow, (iv) maximum volume available, and (v) small gap limit, e.g., due to gap offset errors. The exact locations of the boundaries will shift depending on the fluid properties and instrument used, but their shapes will not change. Representative values are used in Fig. 6.15 for aqueous fluids. Specific equations for boundary lines come from consideration of each limit. The minimum torque, item (i), is set either by the instrument specification (Sect. 3.1) or surface tension torque which becomes increasingly important at small gaps (Sect. 3.4). Based on the criteria $T > T_{\min}$, where torque from steady viscosity is $T = (\eta\Omega R/h)/F_\tau$, the boundary line is defined by

$$h < \frac{\eta\Omega R}{F_\tau T_{\min}} \tag{6.34}$$

which shows the scaling $h \sim \Omega$ that appears in Fig. 6.15. The instrument limit of maximum velocity, item (ii), is simply set by the criteria

$$\Omega < \Omega_{\max} \tag{6.35}$$

and therefore appears as a vertical line in the figure. The limit of secondary flow, item (iii), was discussed in Sect. 3.3. There, a maximum Reynolds number $\mathrm{Re}_{\max}$ sets the boundary line and is based on the definition $\mathrm{Re} = \frac{\rho \Omega h^2}{\eta}$ for parallel disks. Then, the criteria $\mathrm{Re} < \mathrm{Re}_{\max}$ can be written

$$h < \left(\frac{\mathrm{Re}_{\max} \eta}{\rho \Omega} \right)^{1/2} \tag{6.36}$$

which shows the scaling $h \sim \Omega^{-1/2}$ seen in the top right of Fig. 6.15. The last two criteria come from this section, considering small volume and small gap limitations. The volume limit is simply $V < V_{\max}$ where $V_{\max}$ is the maximum sample volume available. For parallel disks, $V = \pi R^2 h$, and the boundary line is defined by

$$h < \frac{V_{\max}}{\pi R^2}. \tag{6.37}$$

The final boundary, item (v), is the minimum gap. This boundary line is defined by

$$h > h_{\min}, \tag{6.38}$$

where $h_{\min}$ is set by the gap offset error, or possibly the minimum gap where confinement effects are negligible and the material can still be considered a continuum. Figure 6.15 uses Eqs. 6.34–6.38 with representative parameters given in the caption. The minimum gap $h = 10$ μm is used, assuming uncertainty in gap error much less than 10 μm which would allow for gap offset corrections. Based on the maximum sample volume and minimum gap limits, the experimental window is confined between $h = 10 - 100\,\mu$m for this example. If larger volumes are available, then larger gaps can be used, eventually being limited by the secondary flow (e.g., as seen in Fig. 6.14 at larger gaps). At very large gaps, the experimental window closes. This occurs where the minimum torque and secondary flow boundaries intersect, for gaps $h > 1{,}000\,\mu$ m with this particular geometry.

3.8 Other Issues

Additional challenges, basic and exotic, can also be included on the list of possible ways that rheological measurements can go astray.

One basic but important point is sample volume underfill or overfill. In cone-plate and parallel disk geometries, torque is a very sensitive function of the radial extent of contact $T \sim \frac{1}{R^3}$ [8]. Underfill is more sensitive than overfill, but for

both cases one may have the problem of an uncontrolled contact line that loses rotational symmetry which can introduce additional torque due to surface tension forces (Sect. 3.4). Underfill can also develop as a sample evaporates. This is relevant to aqueous biological fluids. Evaporation can be eliminated or reduced by the use of a solvent trap. The use of a micropipette and close attention to fill level can further eliminate the basic issue of sample volume underfill or overfill.

An exotic but relevant issue with some biological fluids is particle settling and migration, in particular with active-swimming microorganisms in suspension. In general, the concentric cylinder geometry is recommended when gravitational particle settling may be an issue, since a depletion layer is not created across the velocity gradient direction as would be the case with cone-plate or parallel disk geometries. But, if the sample volume is not sufficient, parallel disks or the cone-plate geometry must be used. One particularly striking example is with the same microalgae suspension whose flow data is given in Fig. 6.3. Those measurements were made with a cone-plate geometry. The data needed to be collected within the first 2 min of flow due to microalgae rheotaxis (flow-induced swimming), coupled with particle settling and secondary flow. The microalgae migration was visualized through a transparent bottom plate during shear flow, as shown in Fig. 6.16. The migration to a nonhomogeneous state is indicated by the development of a dark green circle toward the center of the geometry. The particles are negatively buoyant and therefore settle to the bottom fixed plate. A finite secondary flow exists which draws fluid radially outward near the moving cone (Sect. 3.3), which is balanced by a radially inward flow near the stationary boundary. This inward flow carries the negatively buoyant microalgae toward the center. The visualization in Fig. 6.16 indicated the time scale of developing a non-homogeneous sample. This set an experimental boundary on the *time* that could be used to collect steady-state shear data, under 2 min for this configuration.

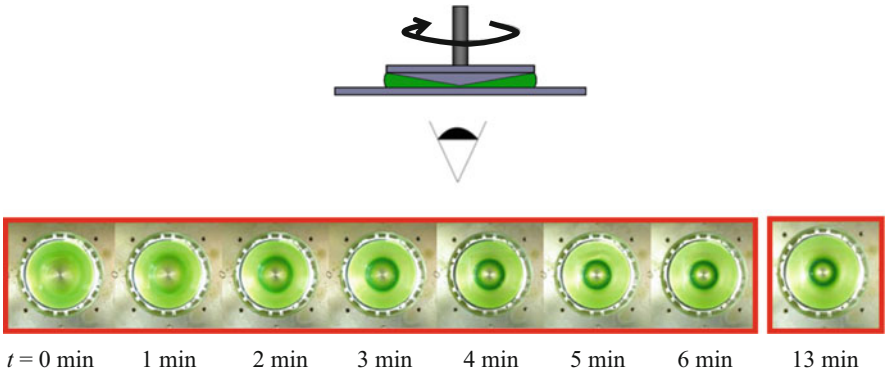

Fig. 6.16 Visualization can be used to check for nonhomogeneous conditions due to rheotaxis, particle settling, and secondary flow. Here, shear flow of a microalgae suspension is viewed from below through a *transparent bottom plate*, showing that a nonhomogeneous distribution develops over time (Previously unpublished work of authors RHE and LMC)

An issue relevant to biological gels, and stiffer biological materials, is edge fracture. This is a well-studied phenomenon, and polymer melts and solutions have tended to receive the most attention [8, 77, 78]. The problem can be identified by visually monitoring the edge of the sample; the experimental artifact is a decreased load (apparent stress) since the true sample contact area is effectively decreased. There are some experimental configurations that minimize edge fracture artifacts, all of which move the free surface away from the transducer surface. For example, a "plate and cup" or "sea of fluid" geometry has been used [79], as well as partitioned plates with the torque transducer plate set inside the larger geometry plate [80–82].

As materials become more viscous and more stiff, additional problems arise. Of all the remaining possible experimental errors [7, 8], viscous heating and instrument compliance are worth mentioning briefly here.

Viscous heating is an issue with higher viscosity fluids. The symptom is a decrease in the apparent viscosity as a function of shear rate, since higher rates further increase temperature and decrease viscosity. The key dimensionless number to check is the Nahme number [2], which can be interpreted as a ratio of viscosity change due to viscous heating compared to the baseline viscosity. Values near zero indicate negligible viscosity change. Smaller gaps help minimize the heating effect, since they decrease the length of the thermal conduction path. This is most important for liquids with high viscosity and low thermal conductivity. For low-viscosity biological fluids, this is less of an issue.

System compliance is an issue with higher stiffness materials. The problem lies in the possibility of finite movement of a "fixed" boundary due to system compliance, or small but finite movement of the load cell, even with modern force rebalancing transducers [83, 84]. Instrument compliance issues have been identified with the dynamic shear measurement of glycerol [85] and polymer melts [86]. Recommendations have been identified for experimental protocol and instrument design to avoid, minimize, and correct for compliance effects [87]. Instrument compliance errors should be considered for stiff, solid materials, or the short-time data from step strain inputs when material stiffness may also be large.

4 Conclusions

The experimental challenges described here will serve as a checklist for troubleshooting and debugging rheological measurements of complex fluids. These challenges are especially evident with biofluids and biological materials. Common artifacts cause a fluid to inaccurately appear as shear thinning, shear thickening, having frequency dependence, time dependence, or having an elastic modulus, when these behaviors are not actually present in the true intensive material response.

We encourage the reader to think critically about experimental rheological measurements, and to ask appropriate and fair questions about the validity of data (including their own and those published in the open literature). This is particularly relevant for biological complex fluids which are soft, have low viscosity, and may contain active components.

For each potential artifact, the system-level perspective can identify an experimental boundary and/or a method of minimizing the effect (Sects. 3.1–3.8). The focus here has been on the most commonly used technique for measuring shear material functions, i.e., drag flow at the boundary ([8] Chap. 5), especially when imposed by rotational geometries such as parallel disks, cone-plate, or concentric cylinders (Fig. 6.1). Other measurement techniques, including those described in this book (Chap. 1, 3–4), will also benefit from a system-level perspective that acknowledges non-ideal conditions for rheological material function measurement (as in Fig. 6.1). The identification of experimental boundaries (similar to Figs. 6.3, 6.5, 6.6, 6.10, 6.11, 6.14, and 6.15) will be especially relevant to biological fluids and materials that are of limited volume, as well as soft, active, and rheologically complex materials more generally.

Acknowledgements This work was supported by the National Science Foundation under Grant No. CBET-1342408. RHE and LMC acknowledge helpful discussions regarding careful rheological measurements with Prof. Christopher Macosko and Dr. David Giles at the University of Minnesota. RHE also thanks Prof. Gareth McKinley at the Massachusetts Institute of Technology for initial discussions on drawing experimental boundaries for rheological measurements. RHE and LMC also acknowledge Prof. Jian Sheng at Texas Tech University (formerly University of Minnesota) for suggesting the study of actively swimming microalgae suspensions, and Mr. Anwar Chengala for preparing those samples.

Appendix: Material Details: Hagfish Gel and Microalgae Suspension

Hagfish gel serves as an example of an ultrasoft biomaterial gel. It is prepared as in [5, 14] and used in Figs. 6.5, 6.6, and 6.7.

The actively swimming microalgae suspension provides an example of a low-viscosity biological solution and is used in Figs. 6.3 and 6.16. The algal species *Dunaliella primolecta* was used. It is a motile, biflagellated, cell-wall-less, unicellular green algae that does not clump. It has slight negative buoyancy, approximate characteristic diameter 11 μm, and natural concentration on the order of $3 \cdot 10^6$ cells/mL. *Dunaliella Primolecta* (UTEX LB 1000) was obtained from UTEX, The Culture Collection of Algae at the University of Texas at Austin. Nonmotile samples were prepared by adding 2 mL of 4 %wt/vol of formaldehyde in phosphate buffered saline (PBS) solution to 25 mL of the bulk sample. The fixed sample was analyzed under light microscope to ensure it was nonmotile.

References

1. J.M. Dealy, J. Rheol. **39**(1), 253 (1995)
2. R.B. Bird, R.C. Armstrong, O. Hassager, *Dynamics of Polymeric Liquids: Volume 1 Fluid Mechanics*, 2nd ed. (Wiley, New York, 1987)
3. R.G. Larson, *The Structure and Rheology of Complex Fluids* (Oxford University Press, New York, 1999)
4. N. Bharadwaj, J.T. Allison, R.H. Ewoldt, in *ASME 2013 International Design Engineering Technical Conferences and Computers and Information in Engineering Conference* (Portland, OR, 2013), paper DETC2013–13,462
5. R.H. Ewoldt, T.M. Winegard, D.S. Fudge, Int. J. Non-Linear Mech. **46**(4), 627 (2011)
6. R.H. Ewoldt, J. Rheol. **57**(1), 177 (2013)
7. K. Walters, *Rheometry* (Wiley, New York, 1975)
8. C.W. Macosko, *Rheology: Principles, Measurements, and Applications* (Wiley-VCH, New York, 1994)
9. R.L. Powell, in *Rheological Measurement*, ed. by A.A. Collyer, D.W. Clegg, 2nd edn., Chap. 9 (Springer, Dordrecht, 1998), pp. 260–298
10. M.S. Oliveira, R. Yeh, G.H. McKinley, J. Non-Newtonian Fluid Mech. **137**(1–3), 137 (2006)
11. L.E. Rodd, T.P. Scott, D.V. Boger, J.J. Cooper-White, G.H. McKinley, J. Non-Newtonian Fluid Mech. **129**(1), 1 (2005)
12. J. Soulages, M. Oliveira, P. Sousa, M. Alves, G. McKinley, J. Non-Newtonian Fluid Mech. **163**(1–3), 9 (2009)
13. M. Johnston, R. Ewoldt, J. Rheol. **57**(6), 1515 (2013)
14. D.S. Fudge, T. Winegard, R.H. Ewoldt, D. Beriault, L. Szewciw, G.H. McKinley, Integr. Comp. Biol. **49**(1), 32 (2009)
15. C. Baravian, D. Quemada, Rheol. Acta **37**(3), 223 (1998)
16. C. Baravian, G. Benbelkacem, F. Caton, Rheol. Acta **46**(5), 577 (2006)
17. R.H. Ewoldt, G.H. McKinley, Rheol. Bull. **76**(1), 4 (2007)
18. N.Y. Yao, R.J. Larsen, D.A. Weitz, J. Rheol. **52**(4), 1013 (2008)
19. Y.C. Lin, G.H. Koenderink, F.C. MacKintosh, D.A. Weitz, Macromolecules **40**(21), 7714 (2007)
20. P. Sharif-Kashani, J.P. Hubschman, D. Sassoon, H.P. Kavehpour, J. Biomech. **44**(3), 419 (2011)
21. C.P. Broedersz, K.E. Kasza, L.M. Jawerth, S. Münster, D.A. Weitz, F.C. MacKintosh, Soft Matter **6**(17), 4120 (2010)
22. H. Lee, J.M. Ferrer, F. Nakamura, M.J. Lang, R.D. Kamm, Acta Biomater. **6**(4), 1207 (2010)
23. K.M. Weigandt, D.C. Pozzo, L. Porcar, Soft Matter **5**(21), 4321 (2009)
24. S. Suri, C.E. Schmidt, Acta Biomater. **5**(7), 2385 (2009)
25. L.C.E. Struik, Rheol. Acta **6**(2), 119 (1967)
26. M.E. Mackay, C.H. Liang, P.J. Halley, Rheol. Acta **31**(5), 481 (1992)
27. J. Magda, R. Larson, J. Non-Newtonian Fluid Mech. **30**(1), 1 (1988)
28. E.S.G. Shaqfeh, Annu. Rev. Fluid Mech. **28**, 129 (1996)
29. G.H. McKinley, P. Pakdel, A. Öztekin, J. Non-Newtonian Fluid Mech. **67**, 19 (1996)
30. P. Pakdel, G. McKinley, Phys. Rev. Lett. **77**(12), 2459 (1996)
31. J.L. Schrag, J. Rheol. **21**(3), 399 (1977)
32. J.A. Yosick, J.A. Giacomin, W.E. Stewart, F. Ding, Rheol. Acta **37**(4), 365 (1998)
33. C. Storm, J.J. Pastore, F.C. MacKintosh, T.C. Lubensky, P.A. Janmey, Nature **435**(7039), 191 (2005)
34. G.I. Taylor, Philos. Trans. R. Soc. Lond. A. Math. Phys. Character **223**(605–615), 289 (1923)
35. S. Chandrasekhar, *Hydrodynamic and Hydromagnetic Stability* (Dover, New York, 1981)
36. R.G. Larson, Rheol. Acta **31**(3), 213 (1992)

37. ISO, 3219, Determination of viscosity using a rotational viscometer with defined shear rate (1993)
38. H.P. Sdougos, S.R. Bussolari, C.F. Dewey, J. Fluid Mech. **138**, 379 (1984)
39. R.M. Turian, Ind. Eng. Chem. Fund. **11**(3), 361 (1972)
40. B. Meulenbroek, C. Storm, A.N. Morozov, W. van Saarloos, J. Non-Newtonian Fluid Mech. **116**(2–3), 235 (2004)
41. L. Pan, A. Morozov, C. Wagner, P.E. Arratia, Phys. Rev. Lett. **110**(17), 174502 (2013)
42. D.F. Griffiths, K. Walters, J. Fluid Mech. **42**(02), 379 (1970)
43. R.W.G. Shipman, M.M. Denn, R. Keunings, Ind. Eng. Chem. Res. **30**(5), 918 (1991)
44. F.M. Orr, L.E. Scriven, A.P. Rivas, J. Fluid Mech. **67**(04), 723 (1975)
45. M.A. Fortes, J. Colloid Interface Sci. **88**(2), 338 (1982)
46. E.J. De Souza, L. Gao, T.J. McCarthy, E. Arzt, A.J. Crosby, Langmuir **24**(4), 1391 (2008)
47. H.M. Laun, J. Meissner, Rheol. Acta **19**(1), 60 (1980)
48. M.E. Mackay, C.A. Cathey, J. Rheol. **35**(2), 237 (1991)
49. M.E. Mackay, in *Rheological Measurement*, ed. by A. Collyer, D. Clegg, 2nd edn., Chap. 20 (Springer, Dordrecht, 1998), pp. 635–665
50. E. Merrill, Physiol. Rev. **49**(4), 863 (1969)
51. V. Sharma, A. Jaishankar, Y.C. Wang, G.H. McKinley, Soft Matter **7**(11), 5150 (2011)
52. R. Buscall, J.I. McGowan, A.J. Morton-Jones, J. Rheol. **37**(4), 621 (1993)
53. H.A. Barnes, J. Non-Newtonian Fluid Mech. **56**(3), 221 (1995)
54. R. Buscall, J. Rheol. **54**(6), 1177 (2010)
55. A. Magnin, J. Piau, J. Non-Newtonian Fluid Mech. **36**, 85 (1990)
56. P. Ballesta, G. Petekidis, L. Isa, W.C.K. Poon, R. Besseling, J. Rheol. **56**(5), 1005 (2012)
57. A. Yoshimura, R.K. Prudhomme, J. Rheol. **32**(1), 53 (1988)
58. C. Clasen, Rheol. Acta **51**(10), 883 (2012)
59. R.H. Ewoldt, C. Clasen, A.E. Hosoi, G.H. McKinley, Soft Matter **3**(5), 634 (2007)
60. C.S. Nickerson, J.A. Kornfield, J. Rheol. **49**(4), 865 (2005)
61. C.S. Nickerson, J. Park, J.A. Kornfield, H. Karageozian, J. Biomech. **41**(9), 1840 (2008)
62. H.A. Barnes, Q.D. Nguyen, J. Non-Newtonian Fluid Mech. **98**(1), 1 (2001)
63. K. Tan, S. Cheng, L. Jugé, L.E. Bilston, J. Biomech. **46**(6), 1060 (2013)
64. S. Nicolle, J.F. Palierne, J. Mech. Behav. Biomed. Mater. **14**(null), 158 (2012)
65. W. Philippoff, C. Han, B. Barnett, M. Dulfano, Biorheology **7**(1), 55 (1970)
66. S.J. Haward, V. Sharma, J.A. Odell, Soft Matter **7**(21), 9908 (2011)
67. C. Clasen, G.H. McKinley, J. Non-Newtonian Fluid Mech. **124**(1–3), 1 (2004)
68. C. Clasen, B.P. Gearing, G.H. McKinley, J. Rheol. **50**(6), 883 (2006)
69. N. Kojić, J. Bico, C. Clasen, G.H. McKinley, J. Exp. Biol. **209**(Pt 21), 4355 (2006)
70. P. Erni, M. Varagnat, C. Clasen, J. Crest, G.H. McKinley, Soft Matter **7**(22), 10889 (2011)
71. A. Tokarev, B. Kaufman, Y. Gu, T. Andrukh, P.H. Adler, K.G. Kornev, Appl. Phys. Lett. **102**(3), 033701 (2013)
72. R. Få hræus, T. Lindqvist, Am. J. Physiol. **96**(3), 562 (1931)
73. R.W. Connelly, J. Greener, J. Rheol. **29**(2), 209 (1985)
74. E. Andablo-Reyes, R. Hidalgo-Álvarez, J. de Vicente, J. Non-Newtonian Fluid Mech. **165**(19–20), 1419 (2010)
75. G.A. Davies, J.R. Stokes, J. Rheol. **49**(4), 919 (2005)
76. C.J. Pipe, T.S. Majmudar, G.H. McKinley, Rheol. Acta **47**(5–6), 621 (2008)
77. R.I. Tanner, M. Keentok, J. Rheol. **27**(1), 47 (1983)
78. M. Keentok, S.C. Xue, Rheol. Acta **38**(4), 321 (1999)
79. J.S. Vrentas, D.C. Venerus, C.M. Vrentas, J. Non-Newtonian Fluid Mech. **40**(1), 1 (1991)
80. T. Schweizer, J. Rheol. **47**(4), 1071 (2003)
81. S.Q. Wang, S. Ravindranath, P.E. Boukany, Macromolecules **44**(2), 183 (2011)
82. F. Snijkers, D. Vlassopoulos, J. Rheol. **55**(6), 1167 (2011)
83. M.E. Mackay, P. Halley, J. Rheol. **35**(8), 1609 (1991)
84. C.Y. Liu, M. Yao, R.G. Garritano, A.J. Franck, C. Bailly, Rheol. Acta **50**(5–6), 537 (2011)

85. K. Schröter, S.A. Hutcheson, X. Shi, A. Mandanici, G.B. McKenna, J. Chem. Phys. **125**(21), 214507 (2006)
86. T. Schweizer, A. Bardow, Rheol. Acta **45**(4), 393 (2006)
87. S.A. Hutcheson, G.B. McKenna, J. Chem. Phys. **129**(7), 074502 (2008)
88. C. Dutcher, S. Muller, Phys. Rev. E. **75**, 047301 (2007)